Physica Medica 67 (2019) 50–57

Contents lists available at ScienceDirect

Physica Medica

journal homepage: www.elsevier.com/locate/ejmp

Original paper

Positron range effects of ^{66}Ga in small-animal PET imaging

M. Rodríguez-Villafuerte[a,*], E.M. Hernández[a], H. Alva-Sánchez[a], A. Martínez-Dávalos[a], M.A. Ávila-Rodríguez[b]

[a] Instituto de Física, Universidad Nacional Autónoma de México, Mexico City, Mexico
[b] Unidad Radiofarmacia-Ciclotrón, Facultad de Medicina, Universidad Nacional Autónoma de México, Mexico City, Mexico

ARTICLE INFO

Keywords:
microPET
Nonconventional nuclides
Positron range
Spatial resolution
Gallium-66

ABSTRACT

Purpose: Gallium-66 is a non-conventional positron emitter that stands out not only for its high potential to label peptides, proteins and antibodies, but also because it can provide spatio-temporal information of relatively slow physiological processes in the body due to its conveniently long half-life of 9.5 h. However, ^{66}Ga emits the most energetic positrons for PET imaging. The lack of information of the positron range effect on spatial resolution for this positron emitter is an issue, particularly in preclinical imaging.

Methods: The line spread function (LSF) in tissue-equivalent materials with densities between 0.2 and 1.93 g/cm^3 was obtained with ^{66}Ga and ^{18}F. A complementary study with the NEMA NU 4-2008 image quality phantom is also included.

Results: High-energy positrons moving in lower density materials produce far-reaching activity distributions. The LSFs were characterized with Lorentzian-Gaussian fits, with spatial resolution (FWHM) in the 2.14–3.2 mm range, and long tails extending a few tens of mm depending on the material type and density. A narrowing of the LSF was observed for lung-equivalent materials, indicating the lack of enough material for the positron annihilation to take place. The NEMA NU 4-2008 image quality phantom produced blurred images, notoriously observed in the hot and cold cylinders used for evaluation of recovery coefficients (RC) and spill-over ratios (SOR), producing very low RC and very large SOR.

Conclusions: Quantitative PET imaging with the non-conventional ^{66}Ga is hampered due to the large range of its high-energy positrons affecting both spatial resolution and activity concentration quantification.

1. Introduction

Spatial resolution and activity concentration quantification in Positron Emission Tomography (PET) depends on several physical, technical and biological factors. Positrons travel in tissue until they annihilate into two 511 keV photons. It is well known that higher positron-energy results in a longer positron-range. The latter is a physical factor that, together with the non-collinearity of the annihilation photons, degrade the spatial resolution in PET. In fact, positron-range is the main detector-independent contribution to PET imaging blurring. To a large extent, this can be corrected using different techniques (for instance during image reconstruction) if accurate estimates of positron-range are available. However, the existing estimates differ, and the comparison with the scarce experimental data available is not reliable [1]. Therefore, studying the positron-range in different tissues has become of great interest, especially in modern scanners where one of the aims is to refine spatial resolution which, consequently, can have an improvement in image quantification.

Monte Carlo simulations have been developed to characterize the transport of positrons in water, concluding in analytical expressions for conventional radionuclides as ^{18}F, ^{13}N, ^{11}C, ^{15}O [2–4]. Other materials than water have also been simulated [5,6], but an accurate assessment of the consequences of positron-range in PET imaging requires a specific model for each tissue type. Monte Carlo simulations have confirmed that positron-range depends on the electron and physical density of the surrounding media, the positron being more likely to travel long distances in air than in water [7]. In comparison with experimental studies carried out in water [8–10], to our knowledge only few experimental efforts have been related to the study of positron-range in different tissue-equivalent materials [11,12].

Some works have addressed the question of how accurately should positron-range effects be known to produce corrected high-quality PET images of clinical interest and utility [13]. These studies point out the necessity to fully understand and quantify the positron-range effect for each combination of positron emitter and tissue type; once this is achieved and, with the use of appropriate correction algorithms, it is

* Corresponding author at: Instituto de Física, Universidad Nacional Autónoma de México, A. P. 20-364, C. P. 01000, Mexico City, Mexico.
E-mail address: mercedes@fisica.unam.mx (M. Rodríguez-Villafuerte).

https://doi.org/10.1016/j.ejmp.2019.10.024
Received 29 April 2019; Received in revised form 25 September 2019; Accepted 9 October 2019
Available online 24 October 2019
1120-1797/

possible to foresee noticeable changes in image quality. Positron-range correction in image reconstruction is also of great relevance when dealing with small-animal PET studies, or when radionuclides with large positron range are involved [14,15].

The non-conventional PET nuclides that have emerged in the last years offer great opportunities for the development of new radiopharmaceuticals for diagnostic and radiotherapy applications and are an important part of the research that is being currently carried out. Widely successful tests have been performed with conventional radionuclides, producing images of excellent quality and proved quantification capabilities. Unfortunately, this is not the case with high-energy positron emitting radionuclides (such as ^{66}Ga) which raises questions about the ability to provide good quality images, questions that are particularly relevant in small-animal PET scans. Gallium-66 is a non-standard positron emitter that can be used in PET, with interesting characteristics for practical radiolabeling of peptides, proteins and antibodies, whose slower in vivo kinetics do not correspond to the much shorter half-life of ^{18}F [16]. The chemical properties of gallium make it an ideal candidate to label monoclonal antibodies for the detection, staging and therapy of tumors. Furthermore, the convenient 9.5 h half-life of ^{66}Ga may allow tumor imaging procedures with gallium citrate to be performed on the same day it is administered [16,17] as well as a valuable research tool for ligand screening and preclinical imaging beyond 24 h [18].

The most abundant positrons emitted by ^{66}Ga (50%) have the highest energies considered for PET imaging. Evaluating this radionuclide in terms of spatial resolution and its ability to deliver images with high statistical quality and quantification capability is a challenge [19]. It is well known that, for a radionuclide/radiopharmaceutical to have clinical value, it is imperative to verify image quantification in animal models and phantoms, before being applied in human studies. This arises the great interest and necessity of studying the image quality produced with this radionuclide in microPET scans using *ad hoc* phantoms designed for small-animal imaging.

The aim of this work was to measure the effect of positron-range on spatial resolution with a commercial small-animal PET scanner using positron-emitters in two energy extremes: the commonly available ^{18}F (the radionuclide with the lowest positron energy emitted in PET and used throughout in this work as a reference), and the high-energy positron emitter ^{66}Ga. This was achieved with two approaches:

a) A fundamental investigation through the determination of the line spread function (LSF). To fully understand the positron-range effect, tissue-equivalent materials of clinical interest were used (lung inhale and exhale, adipose tissue, solid water, trabecular and cortical bone). Measurements with thermoplastic-polymer ABS, a material widely used for 3D printing and useful for phantom manufacturing, are also included.
b) A practical study of an image quality phantom for small-animal PET imaging.

Since image quality for iterative reconstruction methods depends on reconstruction parameters such as the number of subsets and iterations, only the 2D filtered-backprojection reconstruction algorithm was considered.

2. Materials and methods

2.1. Positron-emitting radionuclides

Gallium-66 has a complex decay scheme with a half-life of 569.4 min decaying to ^{66}Zn, 56% by beta plus and 44% by electron capture, producing positrons, numerous prompt gamma rays, X-rays and Auger electrons in wide energy intervals. The positrons emitted involve transitions from the ^{66}Ga ground state to several ^{66}Zn excited states as well as to its ground state (with a Q value of 5175 keV). The most important contributions are essentially three β^+ decays, with maximum energies of 4153, 924 and 362 keV as shown in Fig. 1 and Table 1 [20,21]. Regarding the prompt gammas, they all are high-energy and could only enter the energy window through Compton scattering, affecting the spatial resolution and increasing the random coincidence events, limiting image quality and quantification [17,22].

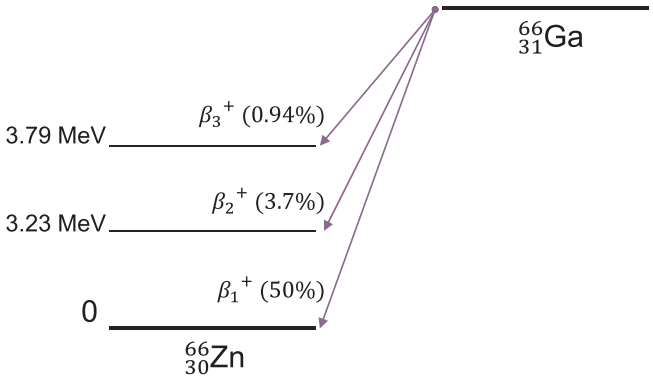

Fig. 1. Simplified β^+ decay scheme of ^{66}Ga to ^{66}Zn, showing the three most important β^+ contributions [20,21].

The ^{66}Ga transitions produce an intricate continuum β^+ energy spectrum, with maximum energy of 4153 keV (Fig. 2) [23]. For comparison, the spectrum produced by ^{18}F ($T_{1/2}$ = 109.8 min, $E_{\beta^+,\,max}$ = 634 keV), the most widely used radionuclide in PET, is also shown.

Both ^{18}F and ^{66}Ga, were produced at the Radiopharmacy-Cyclotron Unit of the School of Medicine at the National Autonomous University of Mexico (UNAM) with 11 MeV protons using an Eclipse HP cyclotron (Siemens Healthcare, Knoxville, TN, USA). The ^{18}F solution was used in the chemical form of FDG from the regular production for clinical applications. Gallium-66 was produced by the ^{66}Zn(p,n) nuclear reaction by methods previously reported [24]. Briefly, isotopically enriched ^{66}Zn (98.72%) was electroplated on Au-baking and bombarded with 11 MeV protons. After bombardment the target material was dissolved with 10 M HCl and radiochemical separation was performed by cation exchange chromatography using AG50W-X4 resin (Bio-Rad, Hercules, CA, USA). After radiochemical purification, the gallium fraction was evaporated to dryness and activity recovered in the chemical form of gallium chloride ($GaCl_3$) with 0.05 M HCl.

2.2. PET studies

Experiments were performed using a microPET Focus 120 (Siemens Preclinical Solutions, Knoxville, TN, USA, previously Concorde Microsystems). A spatial resolution of 1.18 mm (FWHM) using a ^{22}Na point source with a nominal diameter of 0.25 mm has been reported for this small-animal scanner [25]. The activity used in all experiments was measured with a Capintec CRC-15R well-counter. To minimize random coincidence contributions, activities below 5.18 MBq (140 μCi) were used, that produced dead-time values of around 3%.

Due to technical problems with the use of a ^{57}Co long-decayed source, transmission scans for attenuation correction were not performed. It has been reported that the absence of this correction does not affect spatial resolution measurements [26]. However, attenuation reduces activity concentration values measured in the reconstructed PET images, which may influence in the interpretation of the image quality phantom. A further discussion on these issues is presented in Section 2.4.

2.3. Line-sources

Nylon capillary tubes gauge G19 (0.69 mm and 1.08 mm internal and external diameters, respectively, 0.19 mm wall thickness and

Table 1
Physical properties of the most prominent positrons of ^{66}Ga. ^{18}F is included for comparison purposes [20,21].

Radionuclide	Half-life	β^+ probability	Positron energy (keV)		Range in water (mm)	
	(min)	(%)	$E_{\beta^+,mean}$	$E_{\beta^+,max}$	R_{mean}	R_{max}
^{66}Ga	569.4	50.0	1904.1	4153.0	9.3	21.2
		3.7	397.1	924.0	1.3	4.0
		0.94	157.0	362.0	0.3	1.1
^{18}F	109.8	96.7	249.8	633.5	0.6	2.4

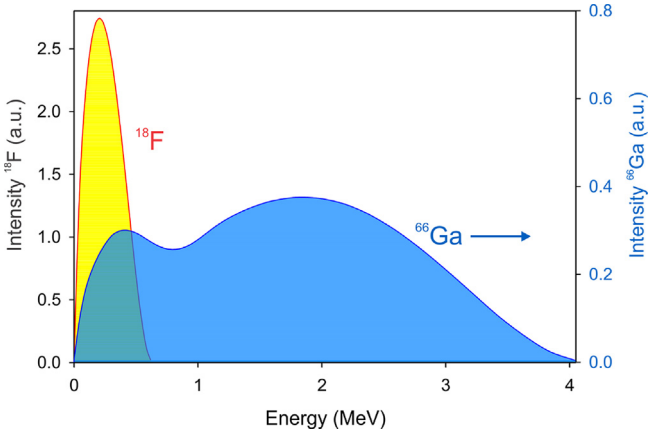

Fig. 2. Theoretical positron energy spectra (normalized to the area under the curve) for ^{18}F and ^{66}Ga. Data from [23].

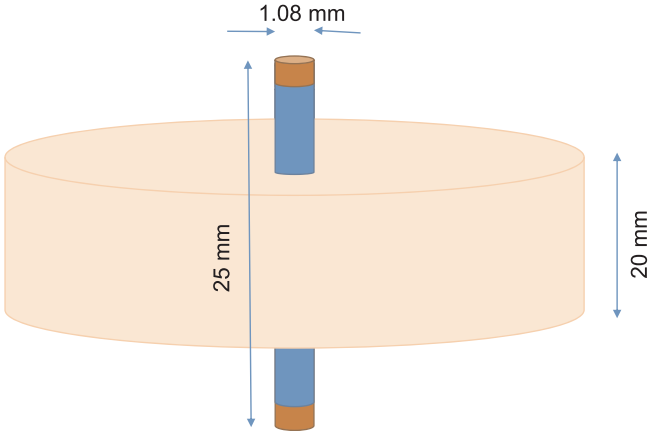

Fig. 3. Diagram of the plastic capillary filled with the radioactive substance inserted at the center of the cylindrical phantoms with different configurations. All the phantoms had 30 mm diameter, except for the lung-equivalent materials, which had a 60 mm diameter.

0.95 g/cm^3 density) were filled with a water solution containing 3.7 MBq/ml (100 μCi/ml) of ^{18}F and 0.93 MBq/ml (25 μCi/ml) of ^{66}Ga at the start of each experiment. The length of the capillary was chosen between 25 and 65 mm depending on the configuration of the phantom. To prevent leakage, the capillary was sealed in both ends with modelling clay.

The line-sources were placed in the middle of tissue-equivalent cylindrical phantoms (Computerized Imaging Reference Systems, Inc., Norfolk, VA, USA), with mass densities in the range of 0.20–1.93 g/cm^3. Table 2 summarizes the most important properties of these materials. The cylindrical phantoms had a length of 20 mm and a diameter of 30 mm, except for the lung-equivalent materials which had a 60 mm diameter. These diameters were chosen to represent a typical mouse-like transaxial dimension (or rat, in the case of the lung-equivalent tissue) as per NU 4-2008 standards [27] where the rodent-like size phantoms are between 25 and 50 mm in diameter. Using phantoms with diameters larger than 60 mm would be unrealistic for small-animal imaging.

The measurements considered the use of only one phantom (i.e. a single material, see Fig. 3) or the combination of different materials, piled up one after the other, to evaluate any effect while increasing the material in the axial direction. The duration of the scans was 20 min with the cylindrical phantoms parallel and centered along the axis of the scanner. An energy window of 350–650 keV was used in all cases.

Table 2
Physical properties of the tissue-equivalent materials and the thermoplastic-polymer (ABS) used in this work. Notice how adipose, solid water, ABS and trabecular bone have very similar density values.

Material	Physical density (g/cm^3)	Density relative to solid water	Electron density ($\times 10^{23}$ e/cm^3)
Lung inhale	0.20	0.19	0.634
Lung exhale	0.50	0.49	1.632
Adipose	0.95	0.93	3.171
Solid water	1.03	1.00	3.333
ABS	1.07	1.04	3.466
Trabecular bone	1.16	1.13	3.730
Cortical bone	1.93	1.87	5.956

2.4. Image quality phantom NEMA NU 4-2008

The NEMA NU 4-2008 protocol [27] was used to evaluate the image quality that can be attained with the microPET Focus 120 in conjunction with i) ^{18}F, as reference, and ii) ^{66}Ga. A mixture of water with 3.7 MBq (100 μCi) of ^{18}F or 5.0 MBq (135 μCi) of ^{66}Ga were used to fill the whole phantom (the fillable volume being approximately 21 ml). The phantom was aligned with the axial direction of the scanner, setting an energy window of 350–650 keV and a 20 min acquisition time.

The image quality (IQ) phantom has several sections designed to evaluate recovery coefficients (RC) and spill-over ratios (SOR). These parameters were calculated as described in the NEMA NU 4-2008 protocol.

Regarding scatter correction, Bahri and collaborators [28] indicate that scatter contamination is low for small rodent studies and should not necessarily be corrected. Certainly, due to the small mouse-size IQ phantom, the scatter fraction is only 11.6% for the experimental conditions used in this study, in particular for the established energy and coincidence windows [25]. Consequently, scatter correction is not compulsory in this case. The effect of the attenuation correction is larger, approximately 20% [29]. Hence, the importance of including the ^{18}F studies as reference. Given that the attenuation of the 511 keV annihilation photons is independent of the positron range (that is, it is an effect independent of the positron emitter), we expect the same attenuation effect in both ^{18}F and ^{66}Ga.

2.5. Image reconstruction parameters

According to the NU 4-2008 standards, the reconstruction should be performed with the method and the parameters recommended by the

manufacturer. However, these recommendations are not given specifically by the manufacturer of the microPET Focus 120 scanner. Therefore, the reconstruction of the tomographic images in all the microPET studies was performed after Fourier rebinning with 2D filtered-backprojection (FBP) using a ramp filter and cut-off frequency of 0.5. Reconstructed PET axial image size was 512 × 512 pixels, with 0.216 mm pixel size and 0.815 mm slice thickness. The choice of using analytical FBP was based on its linearity, allowing easier control of the spatial resolution and noise properties in the reconstruction.

3. Results

3.1. Spatial resolution

To improve statistics, the data of ten contiguous middle tomographic images were averaged along the line-source axis. As established by Alva-Sánchez and collaborators [12] the radial profile of a line-source directly represents the line spread function, $aPSF_{2D}(\delta)$; these distributions were obtained and analyzed for all tissue-equivalent materials.

An interesting feature of the $aPSF_{2D}(\delta)$ for ^{66}Ga is its shape: in all materials these distributions showed a cusp-like peak with long tails of different extensions. To illustrate this, Fig. 4a shows the radial profiles for adipose and cortical bone for both radionuclides (^{18}F and ^{66}Ga) normalized to the maximum intensity at $\delta = 0$ mm. While for ^{18}F and other positron-emitters it is possible to represent the line-source image profiles using double gaussian functions [12,30], in the case of ^{66}Ga the use of a double gaussian did not produce good fits. Instead, the cusp-like profiles required the combination of a narrow Lorentzian and a wide Gaussian function, with the Lorentzian function given by:

$$L(\delta) = \frac{a}{1 + \left(\frac{\delta - \delta_0}{b}\right)^2}$$

This equation involves the determination of two parameters (a and b), assuming $\delta_0 = 0$. Parameter a is the maximum value of the singly peaked function while b is the distance where half its maximum value has been reached ($FWHM = 2b$). The Lorentzian functions for adipose tissue, solid water, ABS, trabecular and cortical bone had a FWHM of 2.64 ± 0.30 mm, while the corresponding Gaussian functions had FWHMs in the 5.6 to 13.8 mm interval. The weighted sum of squared residuals (chi-squared) for these Lorentzian-Gaussian fits were in the 0.002–0.009 range. An example of a Lorentzian-Gaussian function fit to the data for adipose-tissue is shown in Fig. 4b.

According to the standard interpretation [30], the width of the central part of the $aPSF_{2D}(\delta)$ (in our analysis, Lorentzian functions) would be related to the intrinsic scanner resolution and reconstruction algorithm, while the long tails (Gaussians) would be associated with positron range. However, our data show that the Gaussian-shape assumption for the intrinsic scanner resolution and reconstruction algorithm is lost for the high-energy emitting ^{66}Ga as, in this case, the positron range is the dominant effect and cannot be entirely decoupled.

The line-source image profiles normalized to the maximum intensity (at $\delta = 0$ mm) for all materials were plotted using a semi-logarithmic scale (Fig. 5). It can be observed that all materials display a comparable positron-range effect when using the low-energy emitting radionuclide (^{18}F); only the lung-exhale material shows a slightly longer tail. The same behavior of the $aPSF_{2D}(\delta)$ for all materials can be associated to three major contributions: intrinsic scanner resolution, reconstruction algorithm and finite line source diameter, with negligible contribution from positron range. Our results for ^{18}F in water are very similar to those reported by Liu and Laforest [30] in spite of having used different line sources, and have a very good agreement with those reported in [12] for all the tissue-equivalent materials used.

In contrast, the positron-range effect is very drastic for ^{66}Ga, increasing considerably the tails. Their extension covers a range between 8 and 20 mm, depending on the material mass density, confirming that higher energy positrons travelling through lower density materials produce longer tails. These results complement and are in good agreement with previous data reported by our group [12]. However, an unexpected behavior is observed for the two lung-equivalent materials, as there is a narrowing in their shape.

To explore if the $aPSF_{2D}(\delta)$ distributions for ^{66}Ga could present a unified behavior when scaling the radial distance with material density as performed in [1,4], the profiles in Fig. 5 were plotted as a function of $\delta\rho$ where ρ is the material density taken from Table 2. The resulting profiles (not shown) do not overlap after density scaling. This can be explained by considering that our spatial resolution measurements include several contributions besides positron range, namely: scanner resolution, source size, photon non-collinearity and image reconstruction, which do not depend on material density.

It is generally accepted that a description of the $aPSF_{2D}(\delta)$ distributions through their full-width at half-maximum (FWHM), at tenth-maximum (FWTM), at twentieth-maximum (FWTwM) and at fiftieth-maximum (FWFM), gives a convenient measure of the resolution blurring. These parameters were extracted from the data in Fig. 5 using linear interpolation (as indicated in [27]) and presented in Table 3.

To better identify a trend in the data, Fig. 6 shows the resulting values as a function of the tissue-equivalent materials density for both, ^{18}F and ^{66}Ga. The data for ^{18}F clearly shows a gradual enlargement of the $aPSF_{2D}(\delta)$ tails with decreasing material density; this behavior is also observed for ^{66}Ga although the widening of the $aPSF_{2D}(\delta)$ is very severe (note the different vertical-axis scale in the graphs). Once again, a marked change in the tendency of the distribution widths occurs for the lung-equivalent materials owing, most probably, to positrons

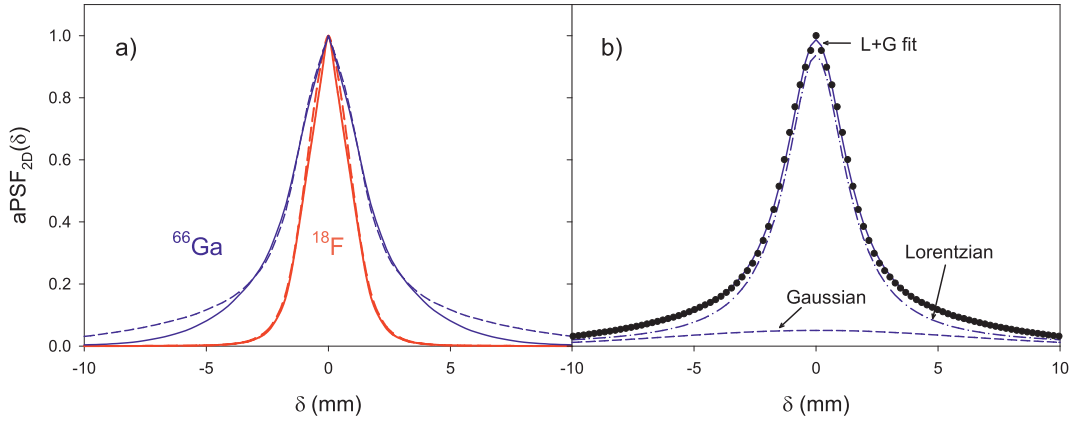

Fig. 4. Normalized $aPSF_{2D}(\delta)$ distributions: a) cortical bone (solid lines) and adipose (dashed lines) tissues for ^{18}F and ^{66}Ga; b) adipose-tissue data for ^{66}Ga together with a nonlinear least-squares fit using the sum of a narrow Lorentzian and a wide Gaussian.

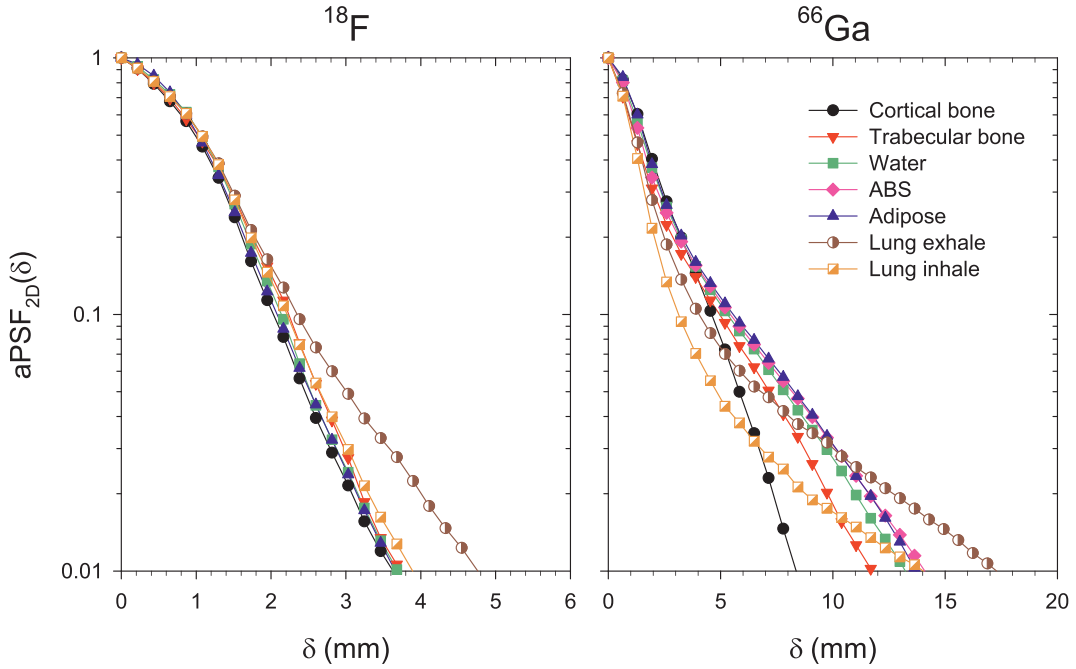

Fig. 5. Normalized aPSF$_{2D}$(δ) functions for ^{18}F (left) and ^{66}Ga (right) for different tissue-equivalent materials.

Table 3
Full-width at half-maximum (FWHM), tenth-maximum (FWTM), twentieth-maximum (FWTwM) and fiftieth-maximum (FWFM) of the aPSF$_{2D}$(δ) distributions for ^{66}Ga and the materials used in this study. Units in mm.

Material	FWHM	FWTM	FWTwM	FWFM
Lung inhale	2.14 ± 0.11	6.3 ± 0.4	9.6 ± 0.4	17 ± 4
Lung exhale	2.42 ± 0.11	8.0 ± 0.4	13.5 ± 0.4	25 ± 2
Adipose	3.12 ± 0.11	11.1 ± 0.2	16.6 ± 0.4	23 ± 4
Solid water	2.98 ± 0.11	10.6 ± 0.2	15.7 ± 0.4	22 ± 3
ABS	2.78 ± 0.11	10.9 ± 0.4	16.4 ± 0.4	23 ± 4
Trabecular bone	2.69 ± 0.11	10.0 ± 0.4	14.5 ± 0.4	20 ± 4
Cortical bone	3.20 ± 0.11	9.2 ± 0.4	11.7 ± 0.4	15 ± 4

traversing longer distances before annihilating.

A compilation of the data reported by our group [12] together with the results presented in this work, offers an excellent opportunity to show the behavior of aPSF$_{2D}$ (in terms of its FWHM, FWTM, FWTwM and FWFM for every tissue-equivalent material) as a function of the positron maximum energy for different radionuclides. This is shown in Fig. 7 for four positron emitters: ^{18}F, ^{13}N, ^{68}Ga and ^{66}Ga with $E_{\beta^+,max}$ of 634, 1198, 1899 and 4153 keV, respectively. It can be observed that, for materials with physical density $\gtrsim$1 g/cm^3, there is a gradual widening of the aPSF$_{2D}$(δ) with increasing β^+ maximum energy; there is up to an order of magnitude difference in the FWFM values compared to the corresponding FWHMs for all the tissue-equivalent materials except lung. This behavior is lost for both types of lung tissue, being more appreciable for lung inhale, with density of only 0.2 g/cm^3. In these two cases (lung inhale and exhale) a compression of the aPSF$_{2D}$(δ) is clearly observed, which can be attributed to positrons exiting the phantoms before annihilation, i.e. there is a lack of material to ensure positron annihilation.

At this point, it is pertinent to discuss the robustness of the spatial resolution results shown in Figs. 5–7 considering the following two aspects:

a. Cylindrical phantom length.
b. Finite scanner spatial resolution.

Cylindrical phantom length. As mentioned in Section 2, the phantom diameters (30 or 60 mm, depending on the material density) were chosen to represent rodent-like size phantoms, all with 20 mm length. Positrons with enough energy traversing a low-density material have a high probability of escaping from the phantom with a partial contribution to the long tails of the distribution. For a very long phantom, compared to the positron range, annihilations detected within a given slice could involve tracks with any direction. For the low-energy positrons emitted from ^{18}F, the phantom is long enough for all the annihilations to take place within the cylindrical volume. This does not necessarily apply for the ^{66}Ga high-energy positrons.

The experimental results from piled-up phantom material for ^{66}Ga did not change the shape nor the extension of the aPSF$_{2D}$ for all materials except both lung tissues. For lung tissues, a slight increase in the extension of the tails was observed, with a maximum difference of 14% in their FWFM. The shape of the curves in Figs. 6 and 7 did not change the trends observed for this type of tissue

This analysis suggests that the limited phantom length had only a small effect in the spatial resolution results for all cases except ^{66}Ga in lung tissue, in which positron range exceeds the phantom dimensions.

Finite scanner spatial resolution. As mentioned previously, the FWHM and FWTM values provide a conventional measure of resolution blurring due to any given factor, including positron range. However, in the case of cusp-like functions (like the ones obtained for ^{66}Ga), these parameters depend on the bin size [2,4]. In this work, the bin size is established by the finite scanner resolution, and the maximum values of the profiles shown in Fig. 5 do not necessarily correspond to the real values due to the smoothing introduced by the bin size. While a smoothing of the cusp will not change the overall shape of the distribution, it will reduce the maximum value and thereby increase the FWxM widths, as these are measured relative to the maximum value. The effect will be determined by the narrowness of the cusp and can therefore depend on the material density. Unfortunately, the real cusp shape cannot be known with precision due to the scanner spatial resolution.

3.2. NEMA NU 4-2008 image quality phantom

Fig. 8 shows the tomographic images corresponding to the spill-over ratio and recovery coefficients sections of the NEMA NU 4-2008 image

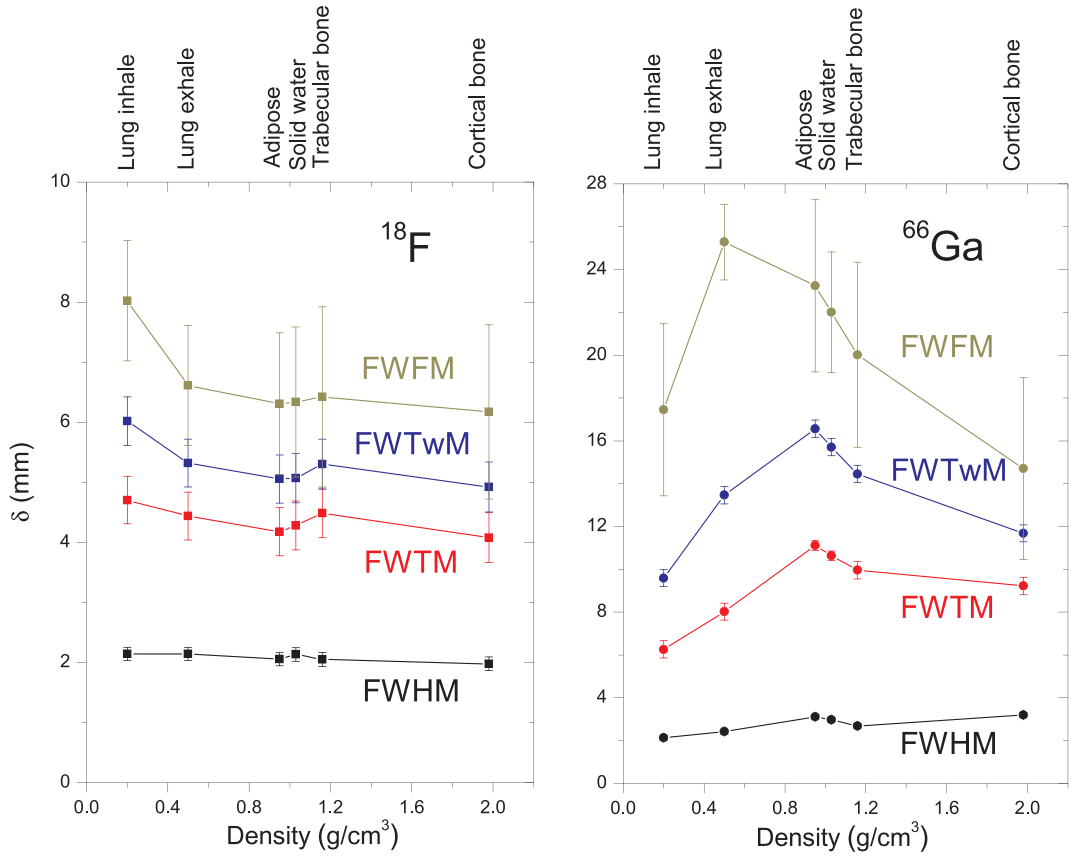

Fig. 6. Full-width at half-maximum (FWHM), tenth-maximum (FWTM), twentieth-maximum (FWTwM) and fiftieth-maximum (FWFM) of the $aPSF_{2D}(\delta)$ distributions as a function of the tissue mass density. Note difference in scales for ^{18}F and ^{66}Ga.

quality phantom for the two radionuclides used in this study. The worsening in image quality is evident when using ^{66}Ga; the substantial blurring introduced by the high-energy positrons of ^{66}Ga makes it very difficult to identify the complete set of hot cylinders; the 2 and 3 mm Ø cylinders can be barely visualized while the 1 mm Ø cylinder is missing. On the other hand, the cold cylinders filled with air and water show an artificial increase in activity.

Taking the air and water cold cylinders, as well as the contour of the uniformity phantom section (not shown) as a reference, the tomographic images for the two radionuclides were registered to aid in identifying the hot-cylinder positions. Regions of interest were delimited for the ^{18}F images as per the NEMA NU 4-2008 protocol instructions [27] and taken as a basis for the evaluation of the recovery coefficients (Fig. 9) and spill-over ratios (Table 4) for the ^{66}Ga images.

Our ^{18}F RC values for all rod diameters are in good agreement with previously reported values [28]. As expected, the RC is close to unity for the 5 mm diameter rod, where the partial volume effect is relatively small. However, for ^{66}Ga only 4 hot-rods were identified (two of them barely); the maximum RC is only 0.43 for the largest cylinder (5 mm diameter), far below unity (the ideal value). The high-energy positron range of ^{66}Ga produced a drastic effect in the spill-over ratios of water and air, with values as large as 0.49 (± 0.03) and 0.27 (± 0.01), respectively. These values are unlikely to be reduced by applying attenuation corrections, since the effect of positron range, with positrons annihilating inside the cold cylinders, is larger than the attenuation of the 511 keV photons in the phantom.

4. Discussion and conclusions

In this work, we investigated the impact that the positron range of the high-energy positron emitter ^{66}Ga has on reconstructed microPET images of line sources (thin capillary tubes) inside cylindrical tissue-equivalent phantoms with mouse-like dimensions. The radial profiles taken from the reconstructed images have a sharp peak with extended tails which required a combined Lorentzian-Gaussian fitting function, from which the FWHM, FWTM, FWTwM and FWFM were obtained and compared to the same LSF measurements performed with ^{18}F (in the latter case, double-Gaussian fits provided a good description). In order to present a sensible interpretation of our results, it is appropriate to separate our analysis into two parts: i) tissue-equivalent materials with densities $\gtrsim$1 g/cm^3, and ii) lung-type tissues. In the first case, while for ^{66}Ga the FWHMs of the narrow Lorentzian fits presented a mean value of 2.64 ± 0.30 mm, the corresponding result (originating from Gaussian fits) for ^{18}F was 1.61 ± 0.14 mm. The comparison of the $aPSF_{2D}$ tails in terms of the FWTwM is more difficult to simplify with a mean value; while for ^{18}F these tails extend to radial distances between 5.0 and 5.3 mm, for ^{66}Ga these values range between 11.7 and 16.6 mm. The widening of the $aPSF_{2D}$ for the high-energy positron emitter, together with the change in the shape of the function that describes its behavior, shows evidence of the large impact that positron range in tissues has with physical density similar or larger than water, being in the case of ^{66}Ga, the dominating factor on the spatial resolution of the reconstructed PET images. The complete set of data for these tissues (FWHM, FWTM, FWTwM, FWFM) allows us to draw two important conclusions:

a. Higher energy positrons moving in lower density materials produce longer tails (Fig. 6). These results agree with previously reported findings.
b. The extension of the tails shows a monotonically increasing behavior with the positron maximum energy (Fig. 7).

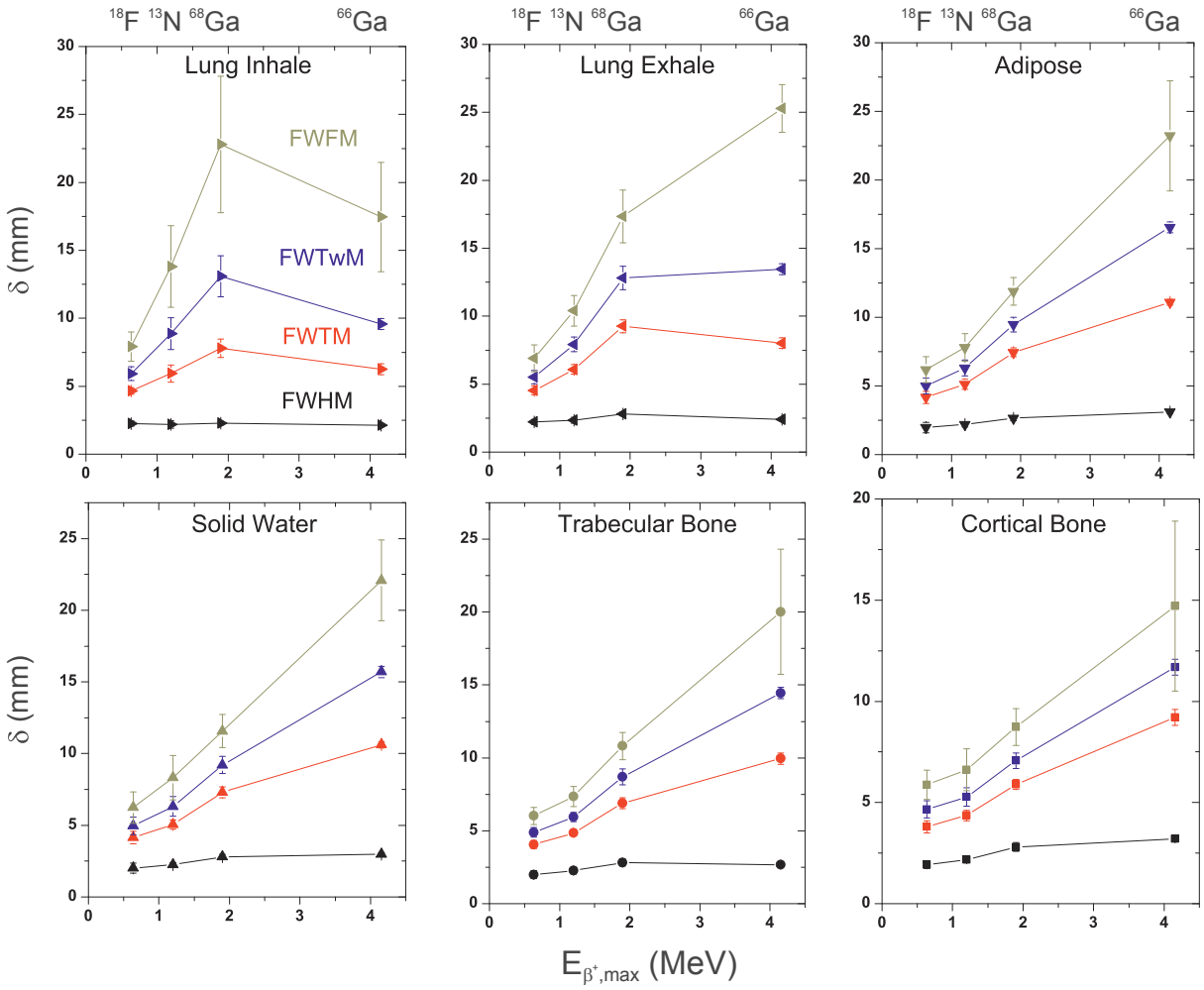

Fig. 7. FWHM, FWTM, FWTwM and FWFM of the $aPSF_{2D}(\delta)$ functions shown in Fig. 5 as a function of the β^+ maximum energy for six tissue-equivalent materials. There is a monotonic widening of the $aPSF_{2D}(\delta)$ as the positron energy increases, except for lung-equivalent tissues.

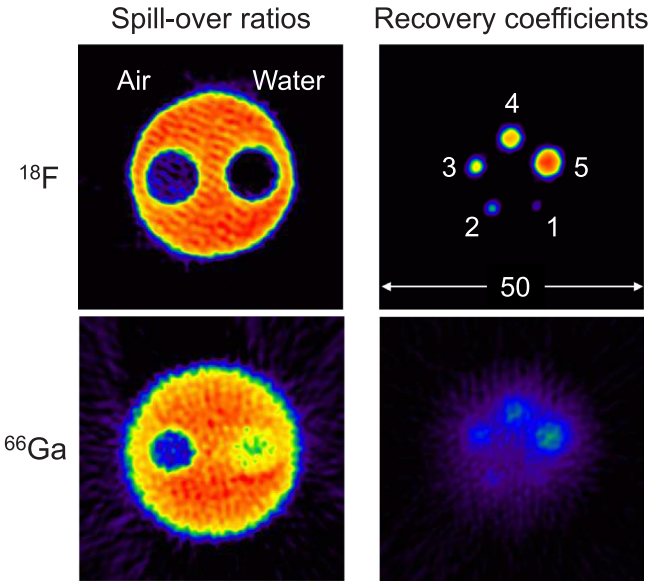

Fig. 8. microPET study of the NEMA NU 4-2008 image quality phantom. The images represent an average of 10 axial slices over the spill-over ratio and recovery coefficients regions, respectively. Dimensions in mm.

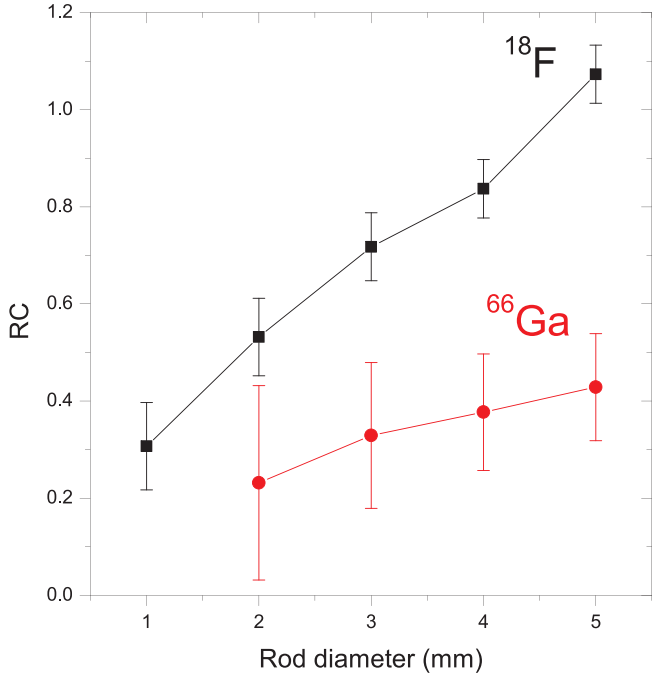

Fig. 9. Recovery coefficients for ^{18}F and ^{66}Ga measured with the NEMA NU 4-2008 image quality phantom.

Table 4
Spill-over ratios for ^{18}F and ^{66}Ga measured in the cold cylinders of the NEMA NU 4-2008 image quality phantom.

Radionuclide	Water	Air
^{18}F	0.04 ± 0.01	0.20 ± 0.03
^{66}Ga	0.49 ± 0.03	0.27 ± 0.01

Our results for the two types of lung and ^{66}Ga show a narrowing of their $aPSF_{2D}$, producing a divergence in the trend observed in the other tissues. This contraction can be attributed, most probably, to positrons traversing longer distances before annihilating. That is to say, there is not sufficient material for the positron annihilations to take place. This hypothesis is sustained by results reported by Kemerink and collaborators [11] for ^{124}I ($E_{\beta^+,max}$ = 2.1 MeV) in lung-equivalent materials. Although their experiment was performed with a clinical PET/CT scanner, the use of foam (as substitute for lung tissue) produced an artefact in the tails of the intensity profiles, which were explained in terms of positrons stopping in dense cardboard surrounding the foam phantom. Our results indicate that ^{66}Ga range distributions degrade the image resolution for all tissues (as demonstrated by the recovery coefficients shown in Fig. 8) and, on the scale of small animals, lung tissue cannot be expected to be resolved at all when this high-energy positron emitter is used.

The plot of our results for conventional (^{18}F, ^{13}N and ^{68}Ga) and non-conventional (^{66}Ga) PET positron emitters provides a very useful means of comparing the expected spatial resolution with positron maximum energy between 0.6 and 4.0 MeV in different tissue-equivalent materials with physical density $\gtrsim$1 g/cm^3. This simple monotonically increasing behavior of the spatial blurring and loss of resolution allows the prediction of the positron-range effect for any other PET nuclide with positron maximum energies within this energy interval.

Although ^{66}Ga is a promising, relatively-long lived radionuclide to label peptides, proteins, and antibodies to image relatively slow physiological processes in the body, its long positron range markedly degrades the attainable spatial resolution, hampering quantitative measurements for small-animal studies, not only affecting spatial resolution but also image quantification. This was demonstrated using the NEMA image quality phantom where the smallest 1 mm diameter hot-rod could not be identified and the recovery coefficients are at least 60% lower than those obtained using ^{18}F in all the other hot-rods.

Acknowledgments

The authors thank Victoria López, Adolfo Zárate, Armando Flores and Fernando Trejo from Unidad Radiofarmacia-Ciclotrón, School of Medicine, UNAM. This work was partially funded by Dirección General de Asuntos del Personal Académico, Programa de Apoyo a Proyectos de Investigación e Innovación Tecnológica, UNAM, Mexico grant IA103418 and Conacyt Atención a Problemas Nacionales, Mexico 2015-01-612.

References

[1] Cal-González J, Herraiz JL, España S, Corzo PMG, Vaquero JJ, Desco M, et al. Positron range estimations with PeneloPET. Phys Med Biol 2013;58:5127–52. https://doi.org/10.1088/0031-9155/58/15/5127.
[2] Levin CS, Hoffman EJ. Calculation of positron range and its effect on the fundamental limit of positron emission tomography system spatial resolution. Phys Med Biol 1999;44:781–99.
[3] Le Loirec C, Champion C. Track structure simulation for positron emitters of medical interest. Part I: the case of the allowed decay isotopes. Nucl Instrum Methods Phys Res Sect Accel Spectrom Detect Assoc Equip 2007;582:644–53. https://doi.org/10.1016/j.nima.2007.08.159.
[4] Jødal L, Loirec CL, Champion C. Positron range in PET imaging: an alternative approach for assessing and correcting the blurring. Phys Med Biol 2012;57:3931. https://doi.org/10.1088/0031-9155/57/12/3931.
[5] Lehnert W, Gregoire M-C, Reilhac A, Meikle SR. Analytical positron range modelling in heterogeneous media for PET Monte Carlo simulation. Phys Med Biol 2011;56:3313–35. https://doi.org/10.1088/0031-9155/56/11/009.
[6] Szirmay-Kalos L, Magdics M, Tóth B, Csébfalvi B, Umenhoffer T, Lantos J, et al. Fast positron range calculation in heterogeneous media for 3D PET reconstruction. 2012 IEEE Nucl. Sci. Symp. Med. Imaging Conf. Rec. NSSMIC 2012. p. 2150–5. https://doi.org/10.1109/NSSMIC.2012.6551492.
[7] Bai B, Ruangma A, Laforest R, Tai Y, Leahy RM. Positron range modeling for statistical PET image reconstruction. 2003 IEEE Nucl. Sci. Symp. Conf. Rec. IEEE Cat No03CH37515 2003. p. 2501–5. https://doi.org/10.1109/NSSMIC.2003.1352400.
[8] Phelps ME, Hoffman EJ, Huang S-C, Ter-Pogossian MM. Effect of positron range on spatial resolution. J Nucl Med 1975;16:649–52.
[9] Cho ZH, Chan JK, Ericksson L, Singh M, Graham S, MacDonald NS, et al. Positron ranges obtained from biomedically important positron-emitting radionuclides. J Nucl Med 1975:1174–6.
[10] Derenzo SE. Precision measurement of annihilation point spread distributions for medically important positron emitters. 5th Int Conf Positron Annihil Lake Yamanaka Jpn. 1979. p. 1–6.
[11] Kemerink GJ, Visser MGW, Franssen R, Beijer E, Zamburlini M, Halders SGEA, et al. Effect of the positron range of ^{18}F, ^{68}Ga and ^{124}I on PET/CT in lung-equivalent materials. Eur J Nucl Med Mol Imaging 2011;38:940–8. https://doi.org/10.1007/s00259-011-1732-1.
[12] Alva-Sánchez H, Quintana-Bautista C, Martínez-Dávalos A, Ávila-Rodríguez MA, Rodríguez-Villafuerte M. Positron range in tissue-equivalent materials: experimental microPET studies. Phys Med Biol 2016;61:6307–21. https://doi.org/10.1088/0031-9155/61/17/6307.
[13] Cal-Gonzalez J, Herraiz JL, Espana S, Desco M, Vaquero JJ, Udias JM. Positron range effects in high resolution 3D PET imaging. 2009 IEEE Nucl. Sci. Symp. Conf. Rec. NSSMIC Orlando, FL: IEEE; 2009. p. 2788–91. https://doi.org/10.1109/NSSMIC.2009.5401950.
[14] Laforest R, Rowland DJ, Welch MJ. MicroPET imaging with non-conventional isotopes. 2001 IEEE Nucl. Sci. Symp. Conf. Rec. Cat No01CH37310 2001. p. 1572–6. https://doi.org/10.1109/NSSMIC.2001.1008638.
[15] Jødal L, Le Loirec C, Champion C. Positron range in PET imaging: non-conventional isotopes. Phys Med Biol 2014;59:7419–34. https://doi.org/10.1088/0031-9155/59/23/7419.
[16] Engle JW, Hong H, Zhang Y, Valdovinos HF, Myklejord DV, Barnhart TE, et al. Positron emission tomography imaging of tumor angiogenesis with a ^{66}Ga-labeled monoclonal antibody. Mol Pharm 2012;9:1441–8. https://doi.org/10.1021/mp300019c.
[17] Graham MC, Pentlow KS, Mawlawi O, Finn RD, Daghighian F, Larson SM. An investigation of the physical characteristics of ^{66}Ga as an isotope for PET imaging and quantification. Med Phys 1997;24:317–26. https://doi.org/10.1118/1.597924.
[18] Amor-Coarasa A, Kelly JM, Ponnala S, Nikolopoulou A, Williams C, Babich JW. ^{66}Ga: a novelty or a valuable preclinical screening tool for the design of targeted radiopharmaceuticals? Molecules 2018;23:2575. https://doi.org/10.3390/molecules23102575.
[19] Laforest R, Non-Conventional PET. Nuclides: production and Imaging. MOMENTO 2015;1. https://doi.org/10.15446/mo.n51.56186.
[20] National Nuclear Data Center. Brookhaven Natl Lab; n.d. https://www.nndc.bnl.gov/ [accessed 27.04.2019].
[21] Radionuclide data tables. Lab Natl Henri Becquerel; 2019. http://www.nucleide.org/DDEP_WG/DDEPdata.htm [accessed 27.04.2019].
[22] Converse AK, Nye JA, Barnhart TE, Dick DW, Avila-Rodriguez MA, Sundaresan R, et al. MicroPET performance in the presence of the third gamma. 2003 IEEE Nucl. Sci. Symp. Conf. Rec. IEEE Cat No03CH37515 Portland, OR, USA: IEEE; 2003. p. 1797–9. https://doi.org/10.1109/NSSMIC.2003.1352227.
[23] Eckerman KF, Westfall RJ, Ryman JC, Cristy M. Availability of nuclear decay data in electronic form, including beta spectra not previously published. Health Phys 1994;67:338–45. https://doi.org/10.1097/00004032-199410000-00004.
[24] Engle JW, Lopez-Rodriguez V, Gaspar-Carcamo RE, Valdovinos HF, Valle-Gonzalez M, Trejo-Ballado F, et al. Very high specific activity $^{66/68}$Ga from zinc targets for PET. Appl Radiat Isot 2012;70:1792–6. https://doi.org/10.1016/j.apradiso.2012.03.030.
[25] Kim JS, Lee JS, Im KC, Kim SJ, Kim S-Y, Lee DS, et al. Performance measurement of the microPET Focus 120 scanner. J Nucl Med 2007;48:1527–35. https://doi.org/10.2967/jnumed.107.040550.
[26] Prieto E, Martí-Climent JM, Arbizu J, Garrastachu P, Domínguez I, Quincoces G, et al. Evaluation of spatial resolution of a PET scanner through the simulation and experimental measurement of the recovery coefficient. Comput Biol Med 2010;40:75–80. https://doi.org/10.1016/j.compbiomed.2009.11.002.
[27] National Electrical Manufacturers Association. NEMA Standard Publication NU 4-2008. Performance Measurements of Small Animal Positron Emission Tomographs. Rosslyn, VA: National Electrical Manufacturers Association; 2008.
[28] Bahri MA, Plenevaux A, Warnock G, Luxen A, Seret A. NEMA NU4-2008 image quality performance report for the microPET focus 120 and for various transmission and reconstruction methods. J Nucl Med 2009;50:1730–8. https://doi.org/10.2967/jnumed.109.063974.
[29] El Ali HH, Bodholdt RP, Jørgensen JT, Myschetzky R, Kjaer A. Importance of attenuation correction (AC) for small animal PET imaging. Diagnostics 2012;2:42–51. https://doi.org/10.3390/diagnostics2040042.
[30] Liu X, Laforest R. Quantitative small animal PET imaging with nonconventional nuclides. Nucl Med Biol 2009;36:551–9. https://doi.org/10.1016/j.nucmedbio.2009.01.019.